Mechanism of the Diels−Alder Reaction Studied with the United Reaction Valley Approach: Mechanistic Differences between Symmetry-Allowed and Symmetry-Forbidden Reactions

Elfi Kraka,* Anan Wu, and Dieter Cremer

Department of Theoretical Chemistry, Göteborg University, Reutersgatan 2, S-41320 Göteborg, Sweden

Received: July 18, 2003

The unified reaction valley approach (URVA) was used to investigate the mechanism of the reaction between ethene and 1,3-butadiene. The reaction valley was explored using different methods (Hartree−Fock, second-order Møller−Plesset perturbation theory, density functional theory (B3LYP), coupled cluster theory (CCSD(T)), and the basis sets 3-21G, 6-31G(d), and 6-311G(d,p). Results were analyzed by characterizing normal modes, the reaction path vector, and the curvature vector in terms of generalized adiabatic modes associated with internal parameters that are used to describe the reaction complex. The Diels−Alder reaction possesses three transition states (TS), where TS1 and TS3 correspond to bifurcation points of the reaction path, at which a C_s-symmetrical reaction complex converts into two C_2-symmetrical reaction complexes. The activation enthalpy at 298 K is 23.5 kcal/mol according to calculations and corrected experimental data. It is determined by a symmetry-supported charge-transfer step, which is followed by a spin-recoupling and a bond formation step. Energy dissipation is strong in the exit channel. Mode selective rate enhancement seems to be not possible for symmetry-allowed reactions, which are characterized by a collective change of many internal coordinates of the reaction complex. Manipulation of the reaction barrier or the reaction mechanism (from concerted to nonconcerted) is only possible in the charge-transfer step. Contrary to opposite claims, aromaticity plays only a minor role for the TS energy.

1. Introduction

In their seminal work, Woodward and Hoffmann demonstrated that concerted pericyclic noncatalyzed reactions can be classified into symmetry-allowed and symmetry-forbidden reactions.[1−3] The latter have a higher reaction barrier than the former because of a symmetry-induced barrier part adding to the electronic reaction barrier. The success of the Woodward−Hoffmann rules in chemistry is well-known and has led to an enormous increase in theoretically based investigations into reaction mechanism. The Woodward−Hoffmann rules are based on state symmetries of reactants and products (state correlation diagram),[1,2] which can be simplified by considering just orbital symmetries (orbital correlation diagram)[1,2] or frontier orbital interactions (PMO diagram).[4] They represent one part of the electronic reality of the reaction mechanism. The question is whether one can develop a theory of the mechanism and the dynamics of concerted pericyclic reactions that is similarly useful as orbital symmetry is but that, as a dynamic analogue of the Woodward−Hoffmann rules, provides a deeper insight into the actual movements and changes in the reaction complex during a symmetry-allowed as opposed to a symmetry-forbidden reaction.

Recently, we investigated the mechanism and the dynamics of substitution, rearrangement, and cycloaddition reactions using the unified reaction valley approach (URVA).[5−9] URVA is based on the reaction path Hamiltonian (RPH) of Miller, Handy, and Adams,[10] the intrinsic reaction coordinate (IRC) of Fukui,[11] and the generalized adiabatic mode concept of Konkoli and Cremer.[12,13] URVA was developed to study the mechanism of a chemical reaction in detail. For this purpose, the reaction path embedded in the reaction valley is explored from the location of the minimum associated with the reactants (in the entrance channel) to the first-order saddle point being the position of the transition state (TS) and, finally, down to the minimum associated with the products (in the exit channel). During this journey all changes in the physical and chemical properties of the reaction complex (RC, the supermolecule made up from the reacting molecules) are monitored so that a detailed account of the reaction mechanism can be given.[5−9]

As far as concerted reactions are concerned, we investigated the symmetry-forbidden [σ^2s + π^2s] cycloaddition reaction of FH to ethene,[7] the [σ^2s + σ^2s] reactions of H_2 + H_2 and FH + FH as well as the [π^2s + π^2s] reaction between two ethene molecules.[9] In this work, we will extend these investigations to a symmetry-allowed reaction, namely, the symmetry-allowed [π^4s + π^2s] reaction between 1,3-butadiene and ethene (Diels−Alder reaction; reaction 1).[14] The mechanism of the Diels−Alder reaction has been investigated from many viewpoints,[1−4] whether it is synchronous or asynchronous, concerted or nonconcerted,[15−17] whether its TS is stabilized by aromaticity in line with the Evans−Dewar−Zimmerman rules[18] and whether this can be confirmed using either susceptibility exaltations[19] or nuclear independent chemical shifts (NICS),[20,21] how its reaction barrier can be lowered or raised,[22] whether it can lead to *trans*-cyclohexene,[23] etc. Furthermore, the retro-Diels−Alder reaction,[24] the hetero-Diels−Alder reaction,[25] or the catalyzed Diels−Alder reaction were investigated.[26] Theory has used the Diels−Alder reaction as a test target for density functional

10.1021/jp030882z CCC: $25.00
Published on Web 09/27/2003

theory (DFT), CASSCF, CCSD(T), and other methods,[15] the use of magnetic properties for the description of TSs,[19−22] the importance of the basis set superposition error,[27] dual level methods in reaction dynamics,[28] etc.

We do not want to add just another quantum chemical study of reaction 1. Instead, we want to answer the fundamental question whether symmetry-allowed and symmetry-forbidden concerted pericyclic reactions differ with regard to their mechanistic and dynamic features in a principal way where reaction 1 is just a suitable example for a symmetry-allowed reaction.

For the purpose of characterizing the mechanism and the dynamics of the Diels−Alder reaction, we will investigate the direction and the curvature of its reaction path because they provide important information on reaction mechanism and reaction dynamics. In the case of a symmetry-forbidden reaction, all chemical processes such as bond breaking and bond forming are indicated by a strong curvature of the reaction path.[7] On the basis of the sequence and the position of the curvature peaks, a transition state region, in which the chemical processes occur, can be distinguished from van der Waals and preparation regions, in which the first interactions of the reaction partners develop and in which the reactants prepare for the actual chemical processes.[5−9] The van der Waals region can be located even if a van der Waals complex does not exist on the potential energy surface (PES).[5,6] The position of the energy TS in the transition state region (early or late) is in line with the Hammond postulate for exothermic or endothermic reactions. The height of the curvature peaks can be related to the strength of the bonds being broken/formed, which has an influence on the reaction barrier and the reaction energy.[5,6] Finally, it is possible to detect hidden intermediates along the reaction path by relating the curvature and other features of the path to structural changes of the reaction complex.[7] Hidden intermediates are transient structures with unique electronic and structural features but which do not occupy a distinct stationary point on the PES. However, they possess electronic features that by variation of the conditions of the reaction (solvent, temperature, substituent influence, etc., which imply a change in the reaction path) lead to a true intermediate occupying a local minimum.[7] In this way, hidden intermediates present an important mechanistic link between different reaction mechanisms observed for different environmental conditions or substitution patterns.

The curvature of the reaction path is related to the curvature couplings,[10] which result from a coupling between the vibrational modes orthogonal to the reaction path and the translational movement of the RC along the reaction path. They provide information on how energy can be transferred from vibrational modes into the reaction path mode and vice versa.[29,30] Knowledge of the curvature couplings can be used for *mode selective rate enhancement*. Similarly, a coupling between vibrational modes along the reaction path leads to energy dissipation during the reaction.[29,30]

The present work will focus on the following questions: (1) Is it possible to identify specific steps along the reaction path of a symmetry-allowed reactions as found for symmetry-forbidden reactions? (2) Does bond breaking and forming take place in the transition state region? (3) Do van der Waals complex, hidden intermediate, or other characteristic structures encountered along the reaction path play an important role for the reaction mechanism. (4) Can the reaction barrier be related to the curvature peaks as found for the symmetry-forbidden reactions? (5) Can one enhance the reaction rate by mode selective energy pumping? (6) Is it possible to predict the influence of environmental changes on the reaction mechanism? (7) Is there a chance to predict the stereochemistry of the Diels−Alder reaction of substituted systems from analysis of the mechanism for the parent reaction complex.? (8) Is there a clear difference in the mechanisms of symmetry-forbidden and symmetry-allowed concerted pericyclic reactions? (9) Can one predict under which circumstances the concerted reaction is replaced by a two-step mechanism? (10) Does the classification of pericyclic reactions used in chemistry make sense from a mechanistic and dynamic point of view?

To answer these questions, the results of this work will be presented in the following way. In chapter 2, the basic features of the URVA method will be shortly summarized and the computational methods used in this work will be described. In chapter 3 features of the reaction path and the reaction valley of the Diels−Alder reaction are analyzed, and in chapter 4 the chemical relevance of this investigation and answers to the 10 questions posed above will be presented.

2. Theory and Computational Methods

URVA can be applied to monitor the mechanistic changes of the RC taking place during the course of the reaction in $(3K-L)$-dimensional configuration space (L, number of overall rotations and translations; K, number of atoms in the RC). This space can be decomposed into the one-dimensional reaction path space and the $(3K-L)$-1-dimensional orthogonal space spanned by the harmonic vibrational modes of the RC thus defining a harmonic $(3K-L)$-1-dimensional reaction valley with the reaction path being located on the valley floor.[5,6,10] On the basis of this concept, the Diels Alder reaction was characterized by analyzing properties being associated with the reaction path $\tilde{\mathbf{x}}(s)$ (energy $E(s)$, geometrical parameters $q_n(s)$, reaction path direction $\mathbf{t}(s)$, forces exerted on the atoms of the RC along the reaction path) and properties being associated with the reaction valley (vibrational frequencies $\omega_{mu}(s)$, adiabatic force constants $k_n^a(s)$, reaction path curvature $\mathbf{k}(s)$ and scalar curvature $\kappa(s)$, mode−mode coupling constants $B_{\mu,\nu}(s)$, curvature coupling coefficients $B_{\mu,s}(s)$). In the following, reaction path, reaction valley, and the properties to be discussed in connection with the URVA study will be defined.

(1) Definition of the Reaction Path. The reaction path $\tilde{\mathbf{x}}(s)$ at a point $\tilde{\mathbf{x}}(s_0)$ can be expressed as a Taylor series in s[31,32]

$$\tilde{\mathbf{x}}(s) = \tilde{\mathbf{x}}(s_0) + \mathbf{t}(s)(s - s_0) + \frac{1}{2!}\mathbf{k}(s)(s - s_0)^2 + \ldots \quad (1)$$

with the arc length s of the path (*reaction path length*) being defined by the differential

$$ds^2 = d\mathbf{x}^\dagger \mathbf{M}\, d\mathbf{x} = d\tilde{\mathbf{x}}^\dagger\, d\tilde{\mathbf{x}} \quad (2)$$

where $\mathbf{M}$ is the diagonal matrix of nuclear masses. The reaction path $\tilde{\mathbf{x}}(s)$ is a function of the 3K mass-weighted Cartesian coordinates x_i of the RC. Starting at $s = 0$ (position of the TS), the steepest descent path is followed down into the entrance channel $s < 0$ and down into the exit channel $s > 0$. The first derivative of $\tilde{\mathbf{x}}(s)$ with regard to s is the reaction path vector $\mathbf{t}(s)$, which defines the direction of the path, whereas the second derivative of $\tilde{\mathbf{x}}(s)$ with regard to s is the reaction path curvature $\mathbf{k}(s)$. The reaction path is calculated by increasing (or decreasing) the path length from $s = 0$ by suitable step sizes Δs (between 0.01 and 0.02 amu$^{1/2}$ bohr) until reactants or products are

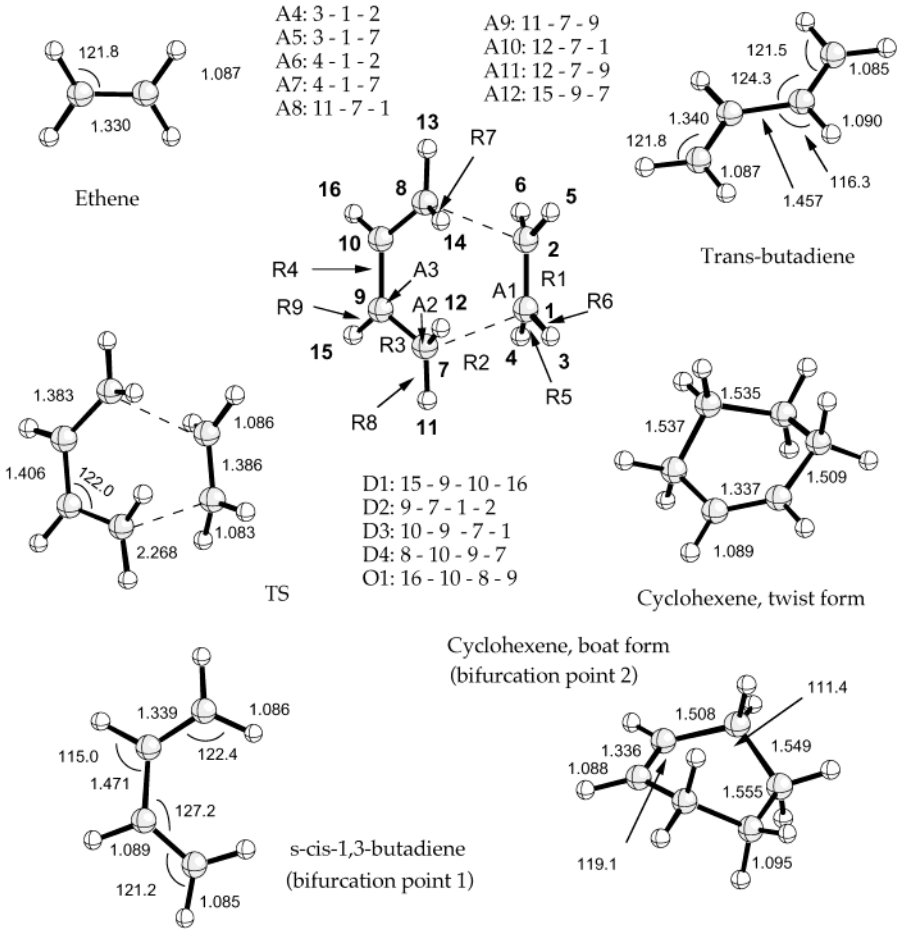

Figure 1. B3LYP/6-31G(d,p) geometries of reactants, TS, and product of reaction 1. Definition of the internal coordinates of the RC. Distances in Å, angles in deg.

reached by exploring the path by suitable path-following algorithms.[6,29−32]

(2) Geometrical Changes along the Reaction Path. The internal coordinates q_n of the RC (for a definition see Figure 1) were calculated as functions of the path length s. Actually, the path following was carried out using Cartesian coordinates. We note in this connection that URVA depends neither on the type of coordinates used to describe the RC nor on whether the reaction path is followed in Cartesian or internal coordinates. The analysis of both path direction and reaction valley is carried out with adiabatic internal modes (AIMs), which are independent of the coordinates used.[12,13]

(3) Analysis of the Reaction Path Direction. For the purpose of determining which internal coordinates dominate the direction of the reaction path, the reaction path vector $\mathbf{t}(s)$

$$\mathbf{t}(s) = \sum_{n=1}^{3K-L} t_n(s)\,\mathbf{u}_n(s) \tag{3}$$

was decomposed into basis vectors $\mathbf{u_n}(s)$

$$\mathbf{u}_n(s) = \mathbf{M}^{-1}\mathbf{b}_n(s) \tag{4}$$

where an element i of $\mathbf{b}_n(s)$ is given by $\partial q_n(\mathbf{x})/\partial x_i$. The calculation of the coefficients $t_n(s)$ is described elsewhere.[5,6] Vectors $\mathbf{u}_n$ in eqs 3 and 4 are internal coordinate modes defined in the one-dimensional space[12] that describes the movement of the RC along the reaction path. For the analysis of $\mathbf{t}(s)$, the amplitude $A_{n,s}(\mathbf{t},s)$ of the internal coordinate mode $\mathbf{u}_n(s)$[12] was used:

$$A_{n,s}(\mathbf{t},s) = \frac{[\mathbf{g}(s)^{\dagger}\mathbf{M}(s)^{-1}\mathbf{b}_n(s)]^2}{[\mathbf{g}(s)^{\dagger}\mathbf{M}(s)^{-1}\mathbf{g}(s)][\mathbf{b}_n(s)^{\dagger}\mathbf{M}(s)^{-1}\mathbf{b}_n(s)]} \tag{5}$$

($\mathbf{g}(s)$: energy gradient at point s), which includes beside electronic effects the kinetic aspect of the translational motion along the reaction path.

(4) Forces Exerted on the Atoms of the RC along the Reaction Path. The movement of the RC along the path is a direct consequence of the forces exerted on its atoms. By associating these forces with internal coordinates, a direct insight into the changes of the RC as a function of electronic structure changes is provided. For this purpose, the energy gradient given as a function of s is decomposed in terms of internal coordinate forces. Because the internal coordinate, which dominates at a given point s_0, the direction of the reaction path, is known from step 3, the force having the strongest impact on the RC can be identified. Regions of repulsive (force >0) and attractive interatomic forces (<0) can be distinguished.

Although points 1−4 concentrate on a description of the reaction path, the following quantities are used to describe the reaction valley and the coupling between path and valley.

(5) Normal-Mode Frequencies of the RC. The *harmonic* reaction valley is based on the $N_{\mathrm{vib}} = 3K-L-1$ *generalized*

normal modes $\tilde{\mathbf{l}}^{g}_{\mu}(s)$ and their associated frequencies $\omega^{g}_{\mu}(s)$ according to[5,6,10,31,32]

$$V(s,\mathbf{Q}) = V(s) + {}^{1}/_{2}\sum_{\mu=1}^{N_{vib}} k^{g}_{\mu}(s)\cdot[Q^{g}_{\mu}(s)]^{2} \qquad (6)$$

where $k^{g}_{\mu}(s)$ is the *generalized normal mode force constant*, $Q^{g}_{\mu}(s)$ is the *generalized normal mode coordinate*, and $V(s)$ is the energy profile along the reaction path. Changes of the normal-mode frequencies $\omega^{g}_{\mu}(s)$ along s provide a qualitative impression of the changes in the form of the reaction valley and, by this, of the reaction mechanism. The RPH of Miller, Handy, and Adams[10] implies that all avoided crossings between vibrational eigenstates of the same symmetry along the reaction path are properly resolved for the purpose of correctly describing mode−mode couplings and curvature couplings, which are responsible for energy dissipation and energy transfer along the reactions path. A resolution of the (non)crossing points is achieved by the use of the DMO procedure of Konkoli, Cremer, and Kraka,[33] by which a reliable analysis of curvature coupling and mode−mode coupling coefficients (see steps 8 and 10) becomes possible.

(6) Analysis of All Normal Modes in Terms of Adiabatic Internal Modes. Normal modes are by nature delocalized modes, which makes the description of the reaction complex and the reaction mechanism in the language of the chemist difficult. Therefore, all normal modes are decomposed in terms of adiabatic internal modes (AIMs).[12,13] The AIMS are the localized vibrational modes of the internal coordinates of the RC and, by expressing normal modes in terms of AIMs changes of the former can be directly related to structural changes of the RC. For example, decomposition of normal modes into AIMs provides exact information where and how the bond breaking/forming processes take place.[5−9]

The definition and the advantages of AIMS are described in refs 12 and 13 and will not further be discussed here. For URVA, generalized adiabatic internal modes $\mathbf{a}^{g}_{n}(s)$ are determined in the $(3K-L)$-1-dimensional space. For each internal mode $\mathbf{a}^{g}_{n}(s)$ a force constant $k^{a}_{n}(s)$, a mode mass $m^{a}_{n}(s)$, and a mode frequency $\omega^{a}_{n}(s)$[5,6,12,13] are defined

$$(\mathbf{a}^{g}_{n}(s))_{\mu} = \frac{D_{n\mu}(s)}{k^{g}_{\mu}(s)} \Big/ \sum_{\nu=1}^{N_{vib}} \frac{D_{n\nu}(s)^{2}}{k^{g}_{\nu}(s)} \qquad (7)$$

$$k^{a}_{n}(s) = 1/\sum_{\nu=1}^{N_{vib}} \frac{D_{n\nu}(s)^{2}}{k^{g}_{\nu}(s)} \qquad (8)$$

$$m^{a}_{n}(s) = 1/G_{nn}(s) \qquad (9)$$

$$\omega^{a}_{n}(s) = \sqrt{\frac{k^{a}_{n}(s)}{m^{a}_{n}(s)}} \qquad (10)$$

where $D_{n\mu}(s)$ is an element of the **D**-matrix that connects normal coordinates with internal coordinates and $G_{nn}(s)$ is an element of the Wilson **G**-matrix.

For the decomposition of normal modes into AIMs, the amplitudes $A_{n,\mu}(s)$ are used:[5,6,12,13]

$$A_{n,\mu}(\mathbf{l},s) = \frac{[\mathbf{l}^{\dagger}_{\mu}(s)\,\mathbf{F}(s)\,\mathbf{a}_{n}(s)]^{2}}{[\mathbf{a}^{\dagger}_{n}(s)\,\mathbf{F}(s)\,\mathbf{a}_{n}(s)][\mathbf{l}^{\dagger}_{\mu}(s)\,\mathbf{F}(s)\,\mathbf{l}_{\mu}(s)]} \qquad (11)$$

where the force constant matrix $\mathbf{F}(s)$ is calculated as a function of s.

(7) Identification of Vibrational Modes That Are Converted into (or Generated from) Translational or Rotational Modes. In most chemical reactions (with the exception of rearrangement reactions) the number of vibrational modes of reactants, products, and RC will be different. Vibrational frequencies that vanish during the reaction indicate modes that are converted into either rotations or translations of the RC. By decomposing these modes into AIMs it can be clarified which translation or rotation is generated. In the case of the Diels−Alder reaction the number of reactant vibrations is 36 whereas that of RC is 41 and that of the product is 42. There are 2 additional CC stretching, 2 additional CCC bending, and 2 additional ring torsional vibrations for the latter due to the fact that translational and rotational modes of one of the reaction partners are converted into internal modes.

(8) Analysis of the Mode−Mode Coupling Pattern. Energy dissipation during the course of the reaction is characterized by energy transfer from one mode to the other. The magnitude of this transfer is reflected by the mode−mode coupling elements $B_{\mu,\nu}(s)$[5,6,10,32]

$$B_{\mu,\nu}(s) = \tilde{\mathbf{l}}^{g}_{\mu}(s)^{\dagger}[\mathrm{d}\tilde{\mathbf{l}}^{g}_{\nu}(s)/\mathrm{d}s] = -B_{\nu,\mu}(s) \qquad (12)$$

In regions of strongly localized avoided crossings between two vibrational eigenstates, one finds sharp and localized coupling peaks allowing only little energy exchange. However, if the two vibrational eigenstates slowly approach each other and also slowly depart, thus staying together for a relatively large part Δs of the path, energy exchange and an exchange of the character of the vibrational modes can take place. The corresponding mode−mode coupling peak is relatively broad and more delocalized.

(9) Adiabatic Force Constants of the RC along the Reaction Path. The AIM force constants given in eq 8 can be directly used to analyze changes in the electronic structure of the RC, especially changes in bonding. In regions where the internal coordinate in question dominates the reaction path direction, the adiabatic force constant becomes unusually large (often increasing to a maximum value) and reflects the coupling of the corresponding AIM and the motion along the reaction path.

(10) Reaction Path Curvature and the Curvature Coupling Coefficients. The curvature of the reaction path is given by the vector $\mathbf{k}(s)$. However, it is more convenient to investigate the scalar curvature $\kappa(s)$ given as the Euclidian norm of the curvature vector:

$$\kappa(s) = [\mathbf{k}(s)^{\dagger}\,\mathbf{k}(s)]^{1/2} = [\sum_{\mu=1}^{N_{vib}} B_{\mu,s}{}^{2}(s)]^{1/2} \qquad (13)$$

where

$$\mathbf{k}(s) = \mathrm{d}^{2}\tilde{\mathbf{x}}(s)/\mathrm{d}s^{2} \qquad (14)$$

and

$$B_{\mu,s}(s) = \mathbf{k}(s)^{\dagger}\,\tilde{\mathbf{l}}^{g}_{\mu}(s) \qquad (15)$$

Equation 15 defines the *curvature coupling coefficients*. The latter describe the dynamic coupling between the translational motion along the reaction path and the $3K-7$ normal modes orthogonal to the reaction path. These couplings are important for *mode selective rate enhancement* experiments.[29,30] However,

TABLE 1: Energetics of the Diels Alder Reaction[a]

type	molecule	energy E, ΔE	ZPE	enthalpy H, $\Delta\Delta H_f^0(298)$	exp	μ	S	free energy G, $\Delta G(298)$	lowest freq
reactant 1	ethene	−78.593808	32.08	−78.538692		0	52.32	−78.563553	832
reactant 2	*trans*-butadiene	−156.001661	53.53	−155.910750		0	66.07	−155.942140	176
reactants		−234.59474	85.61	−234.44944			118.39	−234.50569	
bifurcation 1	TS1	3.87	87.39	3.27	3.0[b]	0	116.31	3.89	130i[b]
barrier	TS2	22.43	87.99	23.41	23.5	0.39	77.74	35.53	528i
retro-barrier	TS2	64.61	87.99	61.29	63.1	0.39	87.99	60.08	528i
bifurcation 2	TS3	−36.47 (5.71)	72.06	−32.72 (5.11)		0.26	72.06	−18.91 (5.64)	28i
product	cyclohexene	−42.18	91.93	−37.83	−39.6	0.24	73.86	−24.55	166

[a] Absolute energies E (G) and enthalpies H in hartrees, relative energies ΔE, zero point energies (ZPE), relative enthalpies $\Delta\Delta H_f^0(298)$, and relative free energies $\Delta G(298)$ in kcal/mol, dipole moments μ in Debye, entropies S in entropy units, and lowest frequency in cm^{-1}. B3LYP/6-31G(d,p) calculations. For experimental values, see text. The retro-barrier is given relative to the product, as are the values in parentheses concerning bifurcation point 2. [b] Value for *cis*-butadiene is given.[44c]

what is more important, they reflect those regions along the reaction path in which important chemical processes such as bond cleavage, bond formation take place.[5−9] Those regions are characterized by large curvature peaks.

(11) Decomposition of the Reaction Path Curvature in Terms of Adiabatic Mode-Curvature Coupling Coefficients. For the purpose of getting a better understanding of the mechanistical processes, the curvature vector can be analyzed in terms of AIMs utilizing amplitudes $A_{n,s}(\mathbf{k},s)$, which correspond to *adiabatic curvature coupling coefficients*.

$$A_{n,s}(\mathbf{k},s) = \frac{\mathbf{k}(s)^{\dagger}\,\mathbf{M}(s)\,\mathbf{a}_n^{g}(s)}{\sqrt{(\mathbf{a}_n^{g})^{\dagger}(s)\,\mathbf{M}(s)\,\mathbf{a}_n^{g}(s)}} \tag{16}$$

Equation 16 indicates that the coefficients $A_{n,s}$ possess the same dimension as coefficients $B_{\mu,s}$ and become identical to the latter for $\mathbf{l}_\mu^g = \mathbf{a}_n^g$.[5,6]

Due to the fact that six C atoms participate in reaction 1 and that mass-weighted coordinates are used, calculations had to cover a reaction region of 12 $amu^{1/2}$ bohr corresponding to 600−800 points along the reaction path. The reaction valley was followed from the TS to $s = -5.8$ $amu^{1/2}$ bohr (entrance channel) and from the TS to $s = 5.8$ $amu^{1/2}$ bohr (exit channel) where the end points of the path correspond to bifurcation points (see discussion in the next chapter).

URVA was carried out with the Hartree−Fock (HF), second-order Møller−Plesset perturbation theory (MP2),[34] and density functional theory (DFT)[35] using the hybrid functional B3LYP.[36] Various basis sets were employed ranging from minimal to augmented DZ and TZ basis sets such as the 6-31G(d,p)[37] and the 6-311G(d,p) basis set.[38] Reactants, transition state (TS), and product were in addition calculated with higher level methods such as CCSD(T).[39]

All calculations needed for URVA were carried out with the program ADIA, which is a multipurpose package for the analysis of vibrational spectra and carrying out URVA.[5,12,13] ADIA is a part of the ab initio package COLOGNE2003.[40] For the HF, MP2, DFT, and CCSD(T) calculations, the ab initio package GAUSSIAN98[41] was used.

3. Analysis of the Reaction Path and the Reaction Valley of the Diels−Alder Reaction

Calculated energies and geometries of the stationary points of reaction 1 are summarized in Table 1 and Figure 1. Details of the reaction path and the reaction valley of reaction 1 are shown in Figures 2 (energy profile $V(s)$), Figure 3 (changes in the geometrical parameters $q_n(s)$ of the RC), Figure 4 (internal coordinate contributions to reaction path vector $\mathbf{t}(s)$), Figure 5 (internal forces of the RC), Figures 6 and 7 (vibrational frequencies $\omega_\mu^g(s)$ and mode−mode couplings $B_{\mu,\nu}(s)$), Figure 8 (adiabatic force constants $k_n^a(s)$), Figures 9 and 10 (reaction path curvature $\kappa(s)$ and its decompositions into normal modes or AIMs). The analysis along the reaction path is based in Figures 2−5 and that of the $(3K-7)$-dimensional orthogonal vibrational space in Figures 6−10. In those figures, in which a given property of the RC is represented as a function of s, the position of the TS is defined by a dashed vertical line at $s = 0$. The noninteracting reactants ethene and butadiene are located at $s = -\infty$ and the product cyclohexene at a finite positive value of s.

The kinetics of the Diels−Alder reaction was measured in the gas phase over a temperature range of 160 K (between 760 and 920 K).[42] The Arrhenius activation energy was determined to be 27.5 kcal/mol corresponding to a value of 25.1 at 0 K, as found by extrapolation.[42] For 300 K, an Arrhenius activation energy of 26.0 kcal/mol can be predicted, which corresponds to the bimolecular reaction to an activation enthalpy of 24.8 kcal/mol. Considering, however, the high temperatures employed in the kinetic measurements and the fact that the nonconcerted reaction, following a stepwise addition of ethene to butadiene, is probably only 2.7−4 kcal/mol higher in energy,[15] it is likely that a significant fraction of the reacting molecules follows at 760−920 K the nonconcerted, rather than the concerted path, causing in this way an increase in the activation energy. The activation entropy of a stepwise process is much less negative than that of the concerted reaction (Table 1), thus leading to more favorable free energies for the nonconcerted reaction. One can expect that the activation enthalpy $\Delta\Delta H_f^0(298)$ of the concerted reaction 1 is 23−24 kcal/mol, in line with the B3LYP/6-31G(d,p) results obtained in this work (Table 1). Using the heats of formation $\Delta H_f^0(298)$ of ethene (12.45 kcal/mol), *trans*-1,3-butadiene (26.11 kcal/mol), and cyclohexene (−1.08 kcal/mol[43]), we obtain a reaction enthalpy $\Delta\Delta H_f^0(298)$ of 39.6 kcal/mol.

HF theory overestimates the activation enthalpy at 298 K by 10−20 kcal/mol (HF/3-21G: 36.6; HF/6-31G(d): 46.2 kcal/mol) whereas reasonable reaction enthalpies are obtained (HF/3-21G, −38.3; HF/6-31G(d), −38.1 kcal/mol). MP2/6-31G(d) underestimates the activation enthalpy (20.3 kcal/mol) by 3−4 kcal/mol and exaggerates the exothermicity of the reaction (−45.9 kcal/mol) by 7 kcal/mol. CCSD(T)/6-31G(d) results are better giving an activation enthalpy of 27.5 kcal/mol and a reaction enthalpy of −40.2 kcal/mol. However, the best theoretical prediction for the activation enthalpy is obtained at the B3LYP/6-31G(d,p) level of theory (see Table 1): the activation enthalpy of 23.4 kcal/mol is close to the most likely experimental value of 23.5 kcal/mol whereas the reaction

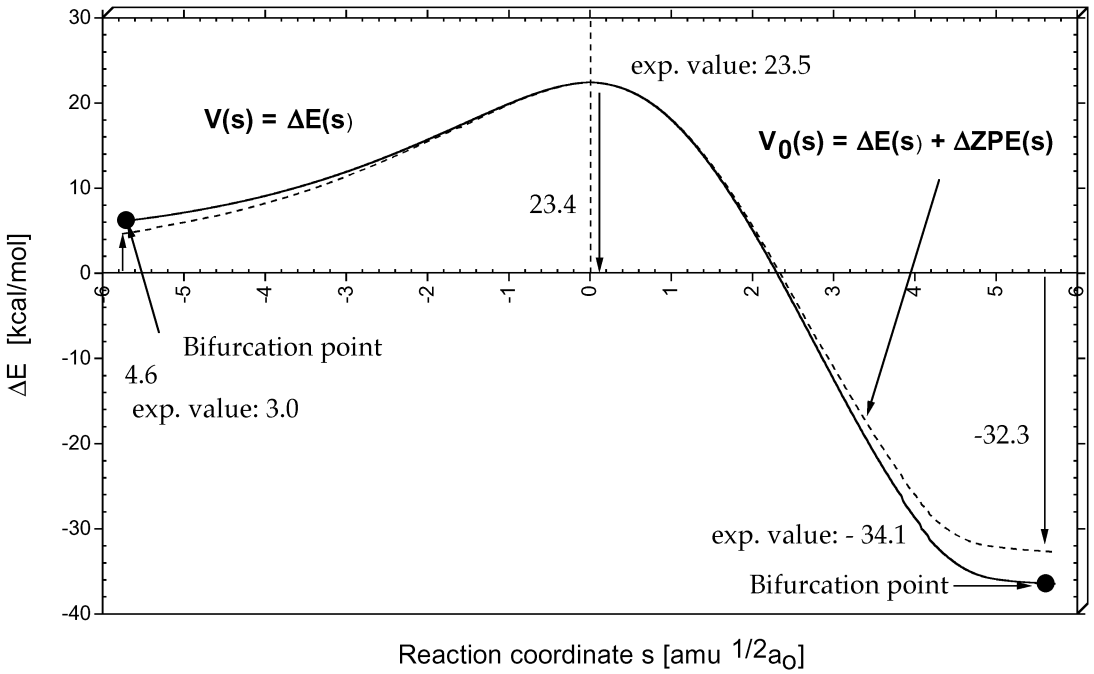

Figure 2. B3LYP/6-31G(d,p) energies $V = \Delta E$ (solid line) and $V_0 = \Delta E + \Delta ZPE$ (dashed line) as a function of the reaction path coordinate s for reaction 1. The position of the TS corresponds to $s = 0$ amu$^{1/2}$ bohr. The energy separation from the reactants and the product is given at the starting and terminating point of the reaction path in kcal/mol.

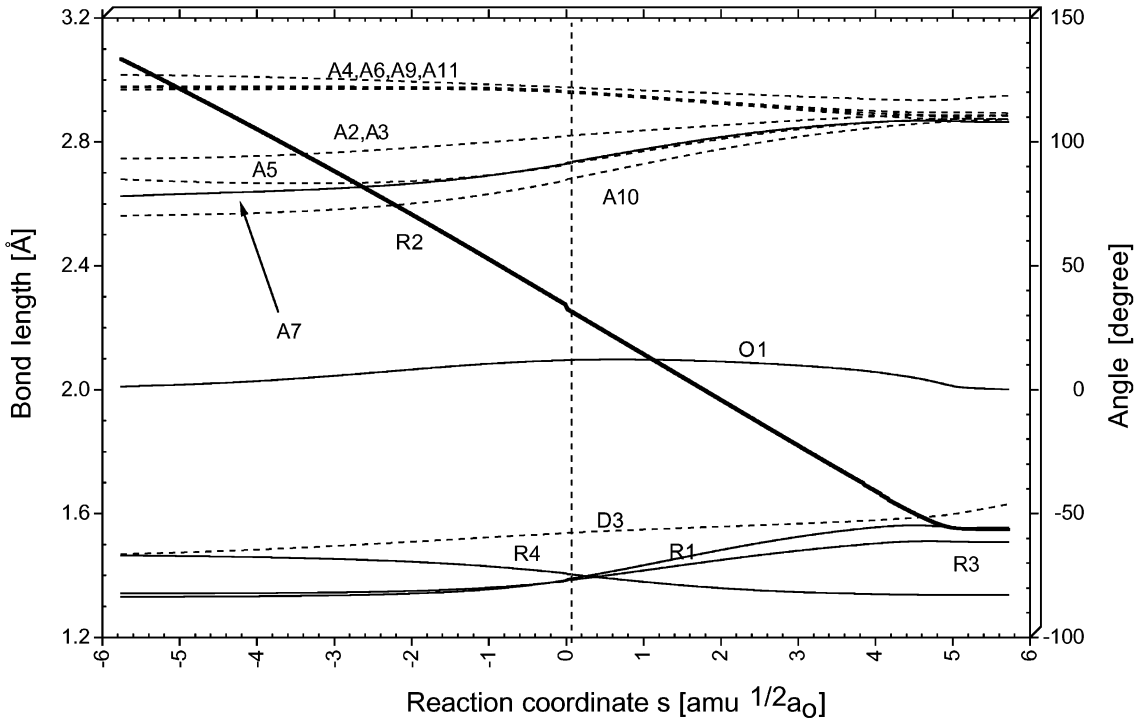

Figure 3. B3LYP/6-31G(d,p) geometrical parameters q_n of the reaction complex RC of (1) given as a function of the reaction coordinate s. For the numbering of internal coordinates, compare with Figure 1. The position of the TS corresponds to $s = 0$ amu$^{1/2}$ bohr and is indicated by a dashed vertical line.

enthalpy (−37.8 kcal/mol) is just 2 kcal/mol above the experimental value of −39.6 kcal/mol. This agreement may, however, be considered as fortuitous because of two reasons. First B3LYP calculations with the larger 6-311G(d,p) basis lead to a higher activation enthalpy of 25.6 kcal/mol whereas the reaction enthalpy (−37.4 kcal/mol) is not improved. Second, it has been shown that corrections for basis set superposition error (BSSE) cannot be neglected and lead to a 0.6 kcal/mol increase in the barrier and a substantial reduction of the exothermicity of the reaction (because of a stabilization of the reactants).[27]

Although the agreement of the B3LYP/6-31G(d,p) data with the available experimental data might be accidental, we present here the B3LYP/6-31G(d,p) URVA analysis and just note that HF and MP2 investigation lead to similar descriptions of mechanism and dynamics of reaction 1. Also we emphasize that geometry and energetics of (1) as obtained in this work have

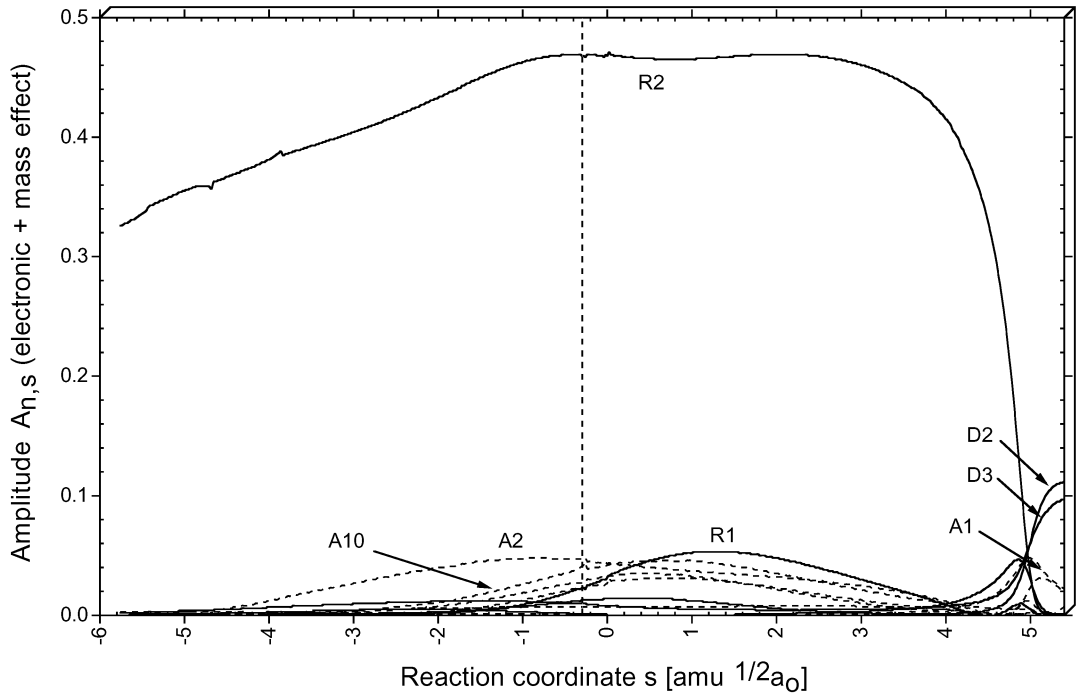

Figure 4. Characterization of the reaction path vector **t**(*s*) of reaction 1 in terms of internal coordinate modes using amplitudes $A_{n,s}$ considering electronic and mass effects according to eq 5. The position of the TS corresponds to $s = 0$ amu$^{1/2}$ bohr and is indicated by a dashed vertical line. B3LYP/6-31G(d,p) calculations.

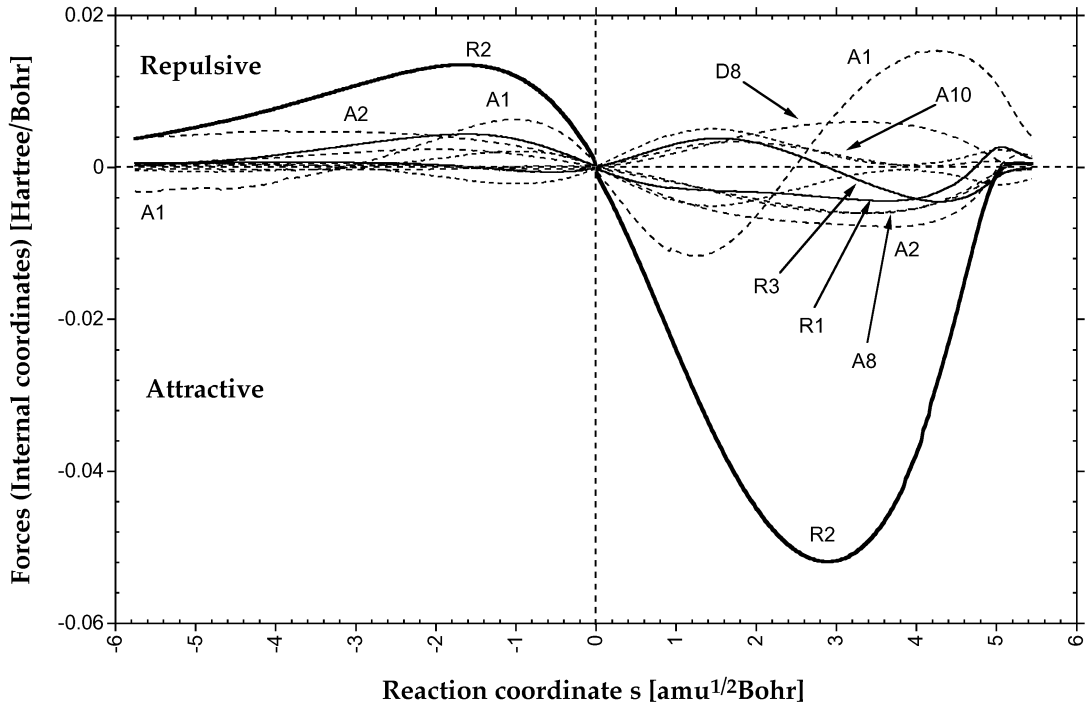

Figure 5. Decomposition of the gradient along the path of reaction 1 in terms of attractive or repulsive internal forces. The position of the TS corresponds to $s = 0$ amu$^{1/2}$ bohr and is indicated by a dashed vertical line. Internal forces associated with the internal coordinates that dominate the direction of the reaction path (compare with Figure 4) are given in bold print. B3LYP/6-31G(d,p) calculations.

also been found by other authors[15,22,23,27] and therefore do not require a detailed description.

In Figure 2, the energy profile $V(s)$ of reaction 1 is described in the range $s = -5.8$ and $s = 5.8$ amu$^{1/2}$ bohr. At $s = -5.8$ amu$^{1/2}$ bohr the RC has approached the energy E of the reactants by 3.9 kcal/mol (Table 1), whereas at $s = 5.8$ amu$^{1/2}$ bohr the RC energy is still 5.7 kcal/mol above that of cyclohexene (Table 1). These differences, however, are misleading as the RC possesses C_s symmetry and can therefore follow the reaction path only as long as this does not get to a bifurcation point from which point on the RC adopts a different symmetry. For example, 1,3-butadiene does not react with its C_{2h}-symmetrical trans equilibrium conformation but only with its C_{2v}-symmetrical cis conformer, which complies with the C_s symmetry of the RC and is 3.9 kcal/mol higher in energy at the B3LYP/6-31G-(d,p) level of theory (experimental value: 3 kcal/mol[44]). Hence, at $s = -5.8$ amu$^{1/2}$ bohr the RC is exactly at the starting point of the C_s-symmetrical reaction path. Similarly, one has to

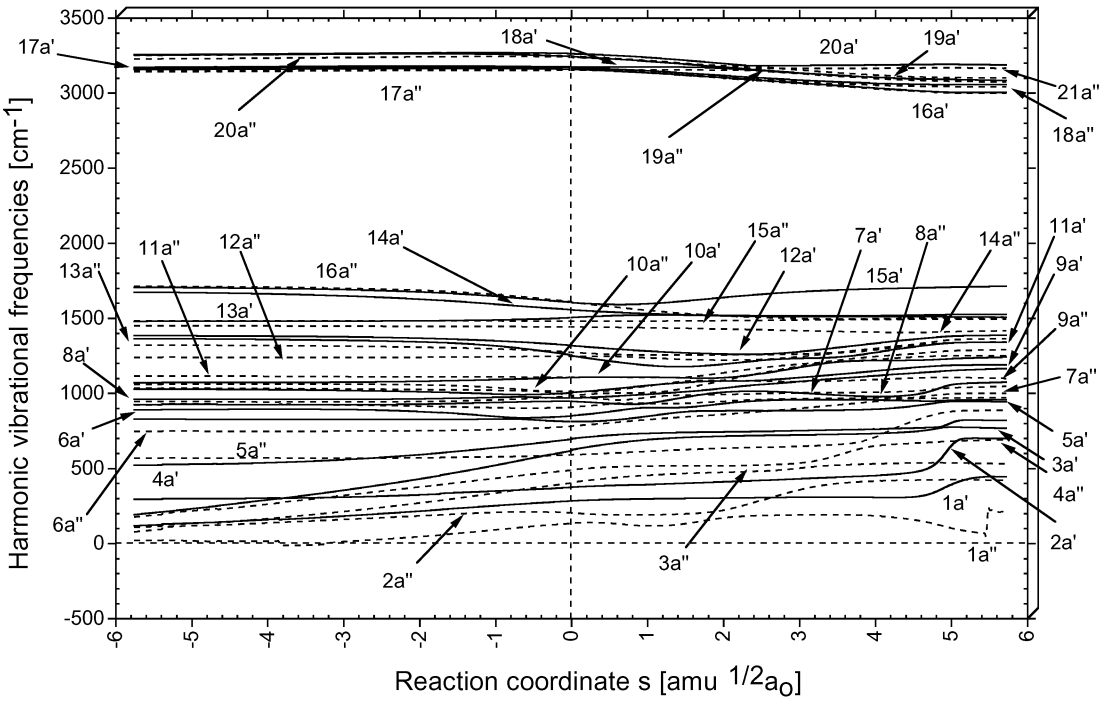

Figure 6. Representation of normal-mode frequencies $\omega_\mu(s)$ of the RC of (1) as a function of the reaction path length s. The position of the TS corresponds to $s = 0$ amu$^{1/2}$ bohr and is given by a dashed vertical line. B3LYP/6-31G(d,p) calculations.

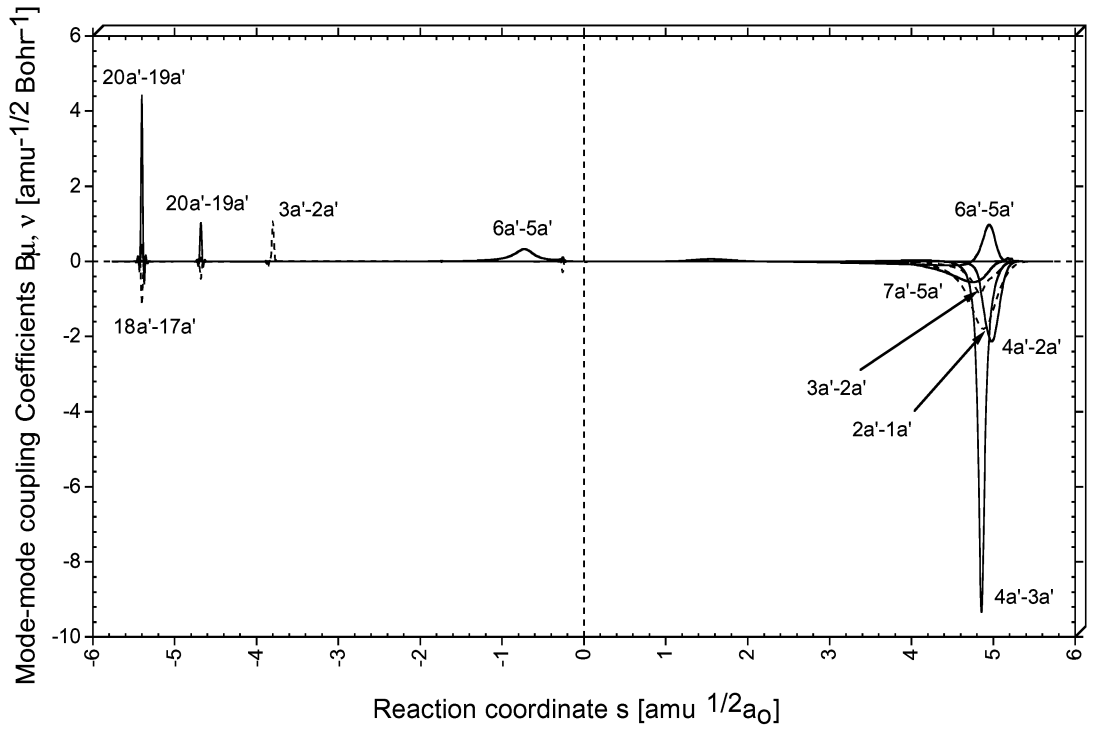

Figure 7. Mode−mode coupling coefficients $B_{\mu,\nu}$ given as a function of the path length s of reaction 1. All 820 mode combinations were considered; however, only the coupling between a'-symmetrical modes is shown. The $B_{\mu,\nu}(s)$ peaks are identified by appropriate normal mode labels (compare with Figure 6). Sharp peaks of $B_{\mu,\nu}(s)$ indicate diabatic energy exchange whereas broad peaks suggest energy dissipation between the corresponding modes. The position of the TS corresponds to $s = 0$ amu$^{1/2}$ bohr and is given by a dashed vertical line. B3LYP/6−31G(d,p) calculations.

consider that cyclohexene prefers a C_2-symmetrical twist conformation, which is 5.7 kcal/mol below the C_s-symmetrical boat conformation[45] into which the RC of reaction 1 is converted. Therefore, $s = 5.8$ amu$^{1/2}$ bohr denotes the bifurcation point, at which cyclohexene converts into its twist form by clockwise or counterclockwise pseudorotation in the equator plane of the cyclohexene globe as was described by Cremer and Szabo.[45] Hence, energy diagram and reaction path of the Diels−Alder reaction are fully described between the two bifurcation points enclosing the important part of the reaction with a C_s-symmetrical RC.

The changes in the geometry of the reaction complex (Figure 3) are dominated by the strong change in the approach parameter R2 (see Figure 1). There are, however, also changes in the bond lengths R1, R3, and R4 as well as the CCC and CCH angles, which approach 109° either from above or below (Figure 3).

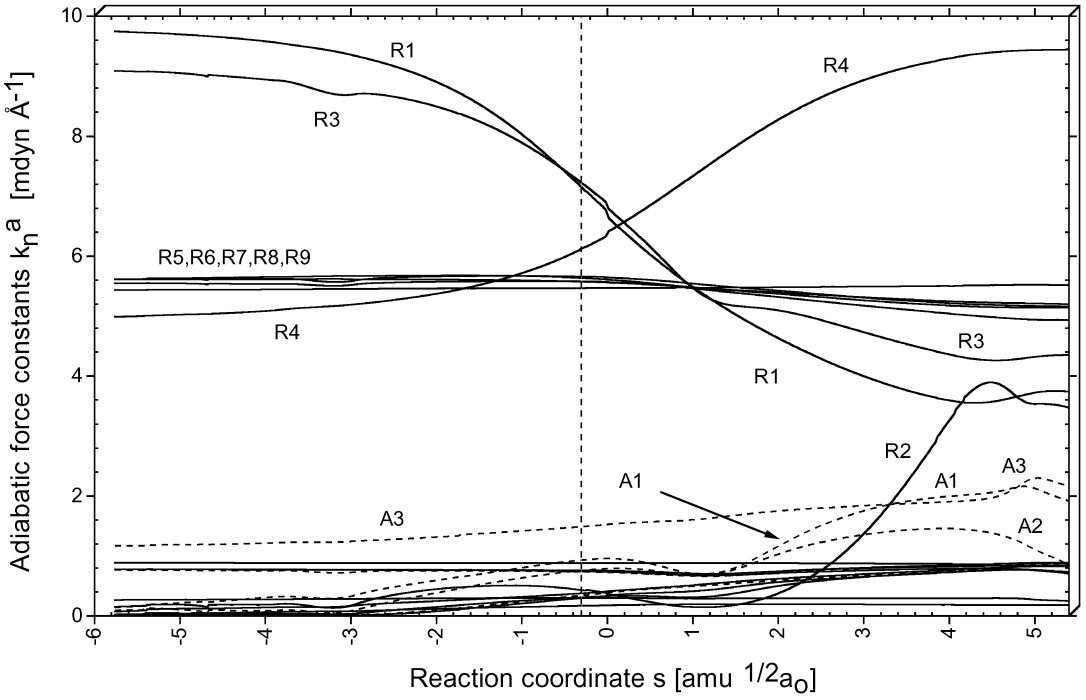

Figure 8. Generalized adiabatic force constants $k_n^a(s)$ associated with the internal parameters q_n given in Figure 1. The position of the TS corresponds to $s = 0$ amu$^{1/2}$ bohr and is indicated by a dashed vertical line. B3LYP/6-31G(d,p) calculations.

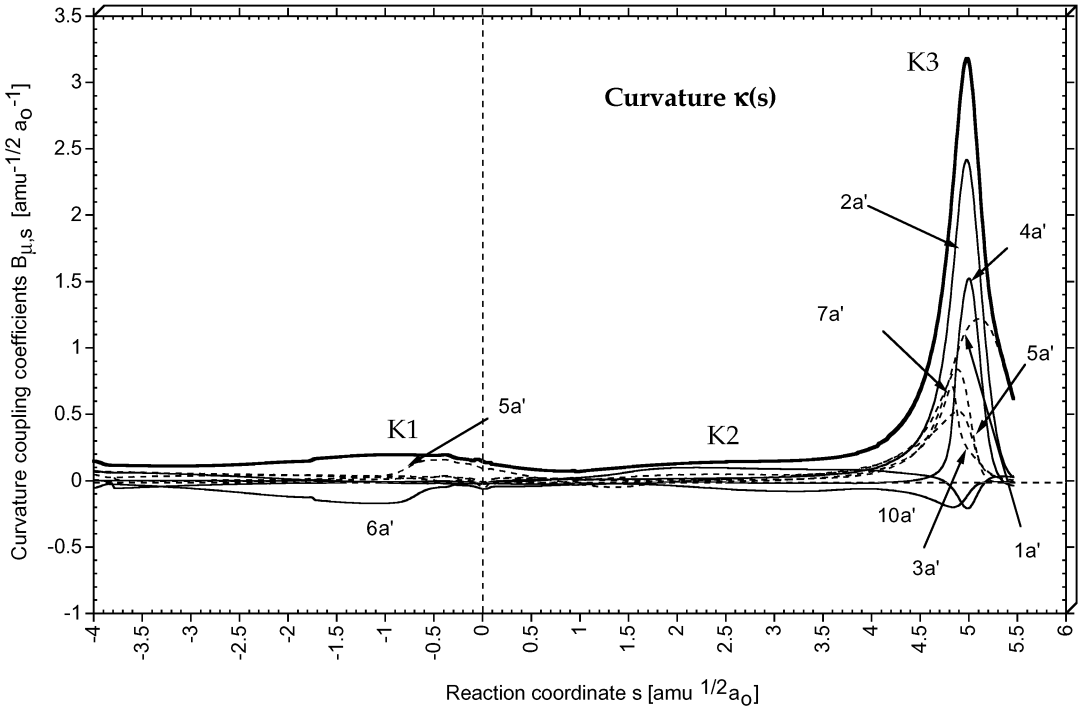

Figure 9. Decomposition of the scalar reaction path curvature $\kappa(s)$ (thick solid line) for reaction 1 in terms of normal mode-curvature coupling coefficients $B_{\mu,s}(s)$ (thin or dashed lines) where the most important modes μ are indicated. Curvature enhancements and peaks are numbered K1, K2, and K3. The position of the TS corresponds to $s = 0$ amu$^{1/2}$ bohr and is indicated by a dashed vertical line. B3LYP/6-31G(d,p) calculations.

The direction of the reaction path vector is clearly dominated by R2 with just minor contributions from R1, R3, R4, and some of the angles (Figure 4). At 5 amu$^{1/2}$ bohr the puckering of the cyclohexene ring starts and dihedral angles D2 and D3 define the direction of the reaction path vector.

Because of the dominance of R2 in determining the direction of the reaction path, the diagram of the internal forces (Figure 5) is easy to read: The approach of the two reactants (described by R2; thick solid line in Figure 5) is slightly repulsive in the entrance channel (because of exchange repulsion) and becomes strongly attractive in the exit channel. Forces associated with R1, R3, and R4 are rather small in the entrance channel and suggest that the two molecules do not strongly resist changes in their geometry. Investigation of the electron density distribution (not shown) reveals that there is a redistribution of negative charge, which results from a mutual charge transfer from HOMO (reactant 1) to LUMO (reactant 2). This charge transfer is possible because of the appropriate symmetry of these orbitals

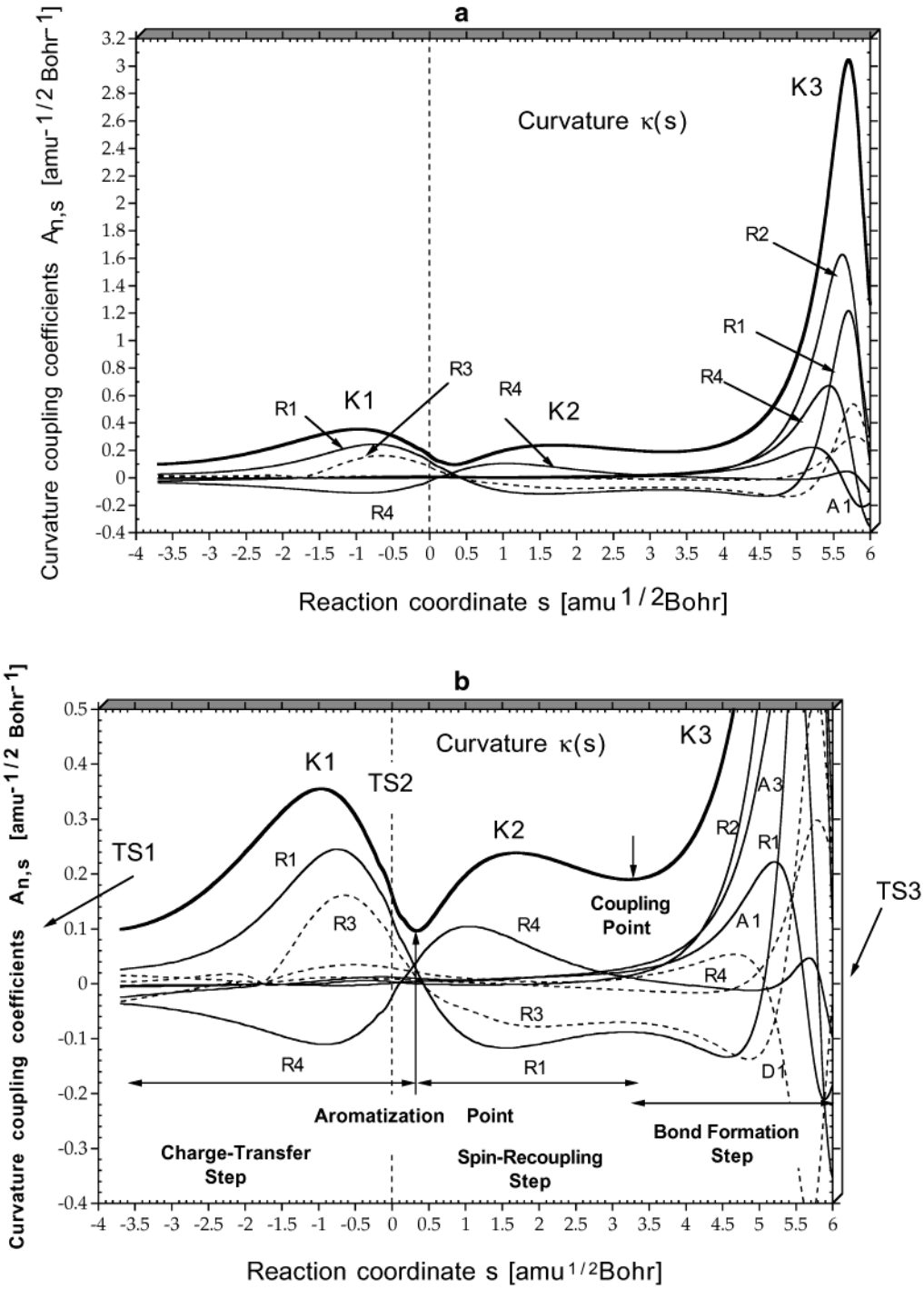

Figure 10. (a) Decomposition of the scalar reaction path curvature $\kappa(s)$ (thick solid line) of reaction 1 in terms of adiabatic mode-curvature coupling amplitudes $A_{n,s}(s)$ (thin solid and dashed lines). (b) The same as (a) but enlarged. Curvature peaks and reaction regions are indicated. The position of the TS corresponds to $s = 0$ amu$^{1/2}$ bohr and is indicated by a dashed vertical line.

and the relatively small HOMO−LUMO gaps.[1−3] The charge transfer leads to a lowering of exchange repulsion (relatively small repulsive R2 force in the entrance channel) and supports the changes in the bond lengths needed to reach the TS geometry (relatively small R1, R3, R4 forces in the entrance channel, Figure 5). It is noteworthy that the R3 forces are first repulsive in the exit channel, supporting lengthening, and then become attractive (at $s = 3$ amu$^{1/2}$ bohr) to hinder further lengthening (Figure 5).

Description of the Reaction Valley. The $3K-7 = 41$ vibrational frequencies of the reaction complex form two bands, a narrow one at 3200 cm^{-1} made up by the CH stretching frequencies and a broad one between 0 and 1700 cm^{-1} (Figure 6). Contrary to a symmetry-forbidden reaction, which is characterized by a large change (1000 cm^{-1} or more) in at least one of the frequencies,[7] there is not a single vibrational frequency that changes strongly. Closer inspection shows, however, that within the two frequency bands there are several frequencies that change by a couple of 100 cm^{-1} (see figures in the Supporting Information). Applying the adiabatic analysis, these changes can be related to changes in bond lengths and bond angles. We refrain from presenting here an analysis of the vibrational frequencies and instead present the mode−mode coupling diagram (Figure 7).

Because of the C_s symmetry of the RC in Figure 7 only couplings $B_{\mu,\nu}(s)$ between the a′-symmetrical vibrational eigenstates are shown because these can lead to a dissipation of the translational energy of the RC into vibrational modes. The coupling peaks indicate the positions of avoided crossings. Narrow and high coupling peaks are characteristic for a short, close contact of the vibrational eigenstates $\omega_\mu(s)$, which leads to an exchange of the energy and the character of one mode to the other (*localized diabatic transitions*). However, such contact is too short to support extensive energy dissipation. The process of energy dissipation occurs when the coupling peaks are broad, indicating that a delocalized avoided crossing provides sufficient opportunity to distribute the energy of one vibrational mode between the two coupling modes. Clearly, the couplings in the exit channel at $s = 4.8$ amu$^{1/2}$ bohr are indicative of energy dissipation between the vibrational modes whereas those in the entrance channel indicate only a simple energy transfer from one mode to the other (Figure 7).

Figure 8 shows the changes of the adiabatic force constants $k_n^a(s)$ along the reaction path. They adopt all normal values (i.e., the none of the internal coordinates of ethene and butadiene couples strongly with the reaction path motion[5,6]). Adiabatic force constants $k_n^a(s)$ associated with R1 and R3 decrease from a typical double bond value at the start to a typical single bond value at the end whereas for the adiabatic force constant associated with R4 the reverse behavior can be observed (Figure 8). There is a point shortly after the TS ($s = 0.2$ amu$^{1/2}$ bohr, Figure 8), at which the adiabatic force constants of R1, R3, and R4 cross. At this point the corresponding CC bonds have the same bond length (1.396 Å, Figure 3) and the same adiabatic force constant ($k^a_{R3=R4}(0.2) = 6.4$ mdyn/Å; actually, the force constant of R1 is slightly shifted to lower values, Figure 8). This observation can be made at all levels of theory and seems to be a typical feature of the reaction mechanism. The adiabatic force constant associated with R2 increases to the single bond value between $s = 3$ and 4.5 amu$^{1/2}$ bohr, indicating that in this region the new CC bonds are formed.

The adiabatic force constants provide insight into the bond strength of the various CC bonds in reactants and product. For example, the CC single bonds next to the CC double bond of cyclohexene (parameter R3) are slightly more stable because of hyperconjugation of the CH_2 groups with the π-bond than the other CC single bonds of cyclohexene (compare $k^a_{R3}(5)$ with $k^a_{R1}(5)$ and $k^a_{R2}(5)$, Figure 8). Furthermore, the CH bonds (apart from R9) become slightly weaker during the reaction (Figure 8).

Reaction Path Curvature. The curvature diagram (Figure 9) looks very different from that of a symmetry-forbidden cycloaddition reaction.[7] There is a large curvature peak K3 far out in the exit channel at $s = 5$ amu$^{1/2}$ bohr whereas before and after the energy TS there are small, flat curvature enhancements (K1 and K2, Figure 9). The curvature couplings are also given; however, they are only of relevance in the region of the large curvature peak. More interesting is the decomposition of the reaction path curvature $\kappa(s)$ into local adiabatic modes (Figure 10a), which is easier to understand, in particular if one uses the enlarged representation of Figure 10b. In the entrance channel of the reaction, all CC bonds of the reaction complex adjust in length, where this is done in a cooperative manner with many small changes but not with a major drastic change, leading to a high curvature peak. The small curvature enhancement before the TS is caused by adiabatic curvature couplings associated with R1, R3, and R4. Shortly behind the TS, where all CC bonds adopt a length of about 1.4 Å, the curvature $\kappa(s)$ adopts a minimum as if a particularly stable point on the PES is reached, which of course is not the case. After the TS, another curvature shoulder develops, again caused by changes in the adiabatic curvature couplings $A_{R1,s}$, $A_{R3,s}$, and $A_{R4,s}$. At $s = 4.5$ amu$^{1/2}$ bohr the amplitude $A_{R2,s}$ starts to increase, thus dominating the curvature peak K3. However, $A_{R1,s}$, $A_{R3,s}$, and $A_{R4,s}$ also contribute to K3 (Figure 10b). It is noteworthy that at both the B3LYP, HF, and MP2 level of theory almost identical curvature diagrams are obtained.

4. Discussion of the Reaction Mechanism: Chemical Relevance of Results

For a symmetry-forbidden reaction such as the addition of FH to the ethene bond, large curvature peaks define a TS region, in which the chemical processes of bond cleavage and bond formation take place. The situation is totally different for the symmetry-allowed reaction. The TS region extends from the first small curvature enhancement at $s = -1$ amu$^{1/2}$ bohr (see enlarged curvature diagram in Figure 10b) to $s = 5.5$ amu$^{1/2}$ bohr, which corresponds to a PES point 58 kcal/mol downhill from the TS. Clearly, peak K3 corresponds to the CC bond formation process leading to cyclohexene and as such it should indicate the end of the TS region, although it is far out in the exit channel. The energy TS would be then very early in the TS region (directly after K1) typical of a strongly exothermic reaction in line with the Hammond postulate.

The first curvature enhancement K1 develops slowly from $s = -3.5$ amu$^{1/2}$ bohr to a maximum value at $s = -1$ amu$^{1/2}$ bohr caused by collective changes in the CC bond lengths, which have lengthened by then by 0.02 Å (R1 and R3) and decreased by 0.025 Å (R4, Figures 1 and 3). R4 is resisting these changes whereas R1 and R3 support these changes, as can be seen from both the force diagram (Figure 5) and the curvature diagram (Figure 10). They change their roles after the minimum in the curvature at $s = 0.2$ amu$^{1/2}$ bohr (Figure 10b). This point indicates a point of CC bond equalization typical of delocalized 6π systems. This suggests that the TS of the Diels−Alder reaction benefits from aromatic stabilization in line with the Evans−Dewar−Zimmerman rules for aromatic and antiaromatic TSs.[18] It seems also to confirm descriptions of the TS using magnetic properties such as the susceptibility exaltation[19] or the NICS values[20] all suggesting aromatic character for TS of a symmetry-allowed reaction such as (1).[21,22]

This is insofar astonishing as R2 is 2.3 Å at the TS, which is far inside the van der Waals distance of 3.6 Å,[46] yet still far outside the region in which strong homoaromatic interactions are encountered (1.9−2.1 Å[47]). At a distance of 2.3 Å, overlap between the π-orbitals is about 0.1, which might lead to some small stabilization through-space.[47] For the purpose of quantifying homoaromatic stabilization at the TS, we calculated the energy of the separated reaction partners calculated in the geometry of the TS considering corrections for BSSEs. At B3LYP the TS was found to be just 2.14 kcal/mol more stable than the noninteracting reaction partners. Hence, there is a weak homoaromatic 6π electron stabilization of the TS; however, this is not the reason for the relatively low barrier of the Diels−Alder reaction. The barrier is a result of the fact that in the area of curvature peak K1 exchange repulsion between the reaction partners is unusually small (Figure 5), which in turn is a result of charge-transfer interactions between the two reactants. Mutual charge transfer involving HOMO and LUMO of the reactants is possible because symmetry and sufficiently small energy differences between HOMO and LUMO guarantee a stabilizing interaction, which leads to a lengthening of double bonds R1

and R3 and a shortening of formal single bond R4. In view of these charge-transfer interactions, it is justified to associate the path region of curvature enhancement K1 with a charge-transfer step (see Figure 10b). The charge-transfer step ends when the (homo)aromatization point is reached.

After the TS and the aromatization point, further shortening of the R4 bond and lengthening of R1 and R3 continues until the π-bonds are fully broken and the butadiene and the ethene molecule have adopted forms with biradical character, out of which a recoupling of electron spins and the formation of the new CC bonds is possible. The region of curvature enhancement K2 is associated with the spin-recoupling step (Figure 10b). After K2, there is another minimum point of the curvature curve $\kappa(s)$ at $s = 3.5$ amu$^{1/2}$ bohr. At this point (R2 = 1.75 Å) the RC starts to form the new CC single bonds (bond formation step, Figure 10b) accompanied by major changes in some of the bond angles. Hence one can distinguish five stages and four specific points of the reaction mechanism with the help of the curvature diagram:

(1) Preparation step associated with an internal rotation of *s-trans*-1,3-butadiene: This step is finished at the bifurcation point TS1 at $s = -5.8$ amu$^{1/2}$ bohr, which is a saddle point of order 1.

(2) Charge-transfer step associated with curvature enhancement K1: Charge-transfer involving the HOMOs and LUMOs of the reaction partners leads to an equalization of all CC bonds to values between 1.396 and 1.400 Å; R2 = 2.3 Å. This step is finished at the aromatization point $s = 0.2$ amu$^{1/2}$ bohr shortly after TS2.

(3) Spin-recoupling step associated with curvature enhancement K2: Formation of two fragments each with biradical character due to a decoupling of the spin of the π-electrons of ethene and butadiene (R2 = 1.75 Å). This step is finished at the coupling point $s = 3.5$ amu$^{1/2}$ bohr (Figure 10b).

(4) Bond formation step associated with curvature peak K3: Formation of the new CC bonds. This step is finished at the second bifurcation point at $s = 5.8$ amu$^{1/2}$ bohr. Again this point is a saddle point of order 1, at which the RC changes from the C_s-symmetrical boat from of cyclohexene into a C_2-symmetrical twist form.

(5) In this last step the most stable cyclohexene form is prepared by following one of two possible pseudorotational paths leading to a C_2-symmetrical twist form.[45]

Hence, the symmetry-allowed Diels−Alder reaction involves three TSs, two of which correspond to path bifurcation points, possessing energies of 3.9 and 5.7 kcal/mol (Table 1) above reactants and product, respectively. There is no van der Waals peak (as found for some of the symmetry-forbidden reactions including polar reaction partners[7]), and therefore, the start of the charge-transfer region coincides with the first bifurcation point.

This partitioning of the reaction mechanism can be considered as being typical of a concerted symmetry-allowed reaction. There are no large curvature peaks close to the energy TS. Instead there is a long charge-transfer region leading to an aromatization of the RC. All geometrical and electronic structure changes in this region take place in a smooth and cooperative manner (determined by the nodal behavior of the frontier orbitals of the reactants), which is more economic and leads to a relatively low energy barrier. We draw a parallel to the pseudorotational mode of a puckered ring, which also involves a collective change of many internal coordinates and accordingly requires a lower energy than ring inversion through a planar form, which requires a drastic change of a few internal coordinates and leads to a higher conformational barrier.[45] The activation energy of reaction 1 is for the preparation of the reactants, whereas the actual formation of the new CC bonds occurs long after the TS and does not require any further energy. Whereas, in a symmetry-forbidden reaction, the energy is needed for the chemical processes of bond breaking and bond forming, the activation energy of a symmetry-allowed reaction is needed for a relatively small collective change in many coordinates of the RC (caused by charger transfer between the frontier orbitals), which is less energy consuming than a single bond cleavage. If the RC has undergone such a collective process, the sequence of follow up changes is no longer energy consuming but energy generating so that the chemical processes are done without any energy barrier far out in the exit channel.

A collective change of many internal coordinates requires less energy and it cannot be accelerated by pumping energy into a particular mode coupling with the reaction path. This can be directly seen from the curvature diagram of Figure 9. It is, however, the question whether the retro-Diels−Alder reaction can be accelerated by pumping energy in mode 2a′, which couples with the reaction path motion (Figure 9). Mode 2a′ couples according to the calculated mode−mode couplings (Figure 7) with mode 4a′, 4a′ in turn with mode 3a′, 3a′ with mode 2a′, and 2a′ with mode with 1a′. Hence, it is likely that the energy supposed to be transferred in the motion of the reaction complex along the reaction path is dissipated between several normal modes and, therefore, of little effect. We conclude that neither for the Diels−Alder nor for the retro-Diels−Alder reaction mode selective rate enhancement plays any significant role.

Clearly, the charge-transfer step decides on the rate of reaction 1. If charge transfer is supported by a strong aromatization effect (e.g., cycloaddition of *o*-quinodimethane with ethene[22]), the aromatization point will move more behind the TS, the TS energy will be lowered, and the reaction becomes more exothermic, in line with the Hammond postulate. Conversely, in a Diels−Alder reaction where the possibility of aromatization is diminished (e.g., reaction with asymmetrically substituted dienes or hetero-dienes/enes), the aromatization point will move before the TS, the TS energy will increase, and the reaction will become less exothermic. Hence, the energy needed for the aromatization step will compete with the energy needed for a single CC bond formation. If the former is larger than the latter, a nonconcerted mechanism will become more likely characterized by an asymmetric TS and two strongly different approach parameters.

In Table 2, the most important differences between the Diels−Alder reaction and some of the symmetry-forbidden reactions investigated previously[7,9] are listed. Clearly some of these differences may result from the fact that the FH + ethene cycloaddition is a reaction that involves a polar reaction partner. However, others will be generally valid and help to answer the 10 questions posed in the Introduction. We have shown that specific points and specific regions along the path of reaction 1 can be distinguished (questions 1 and 3). The symmetry-allowed reaction is characterized by a symmetry-supported charge-transfer step, leading to a collective change of internal coordinates of the RC directed by the nodal behavior of the reactants. Because of the collective change of the internal coordinates, it does not possess large curvature peaks close to the energy TS (questions 2 and 4). The TS region is stretched out into the exit channel and the actual chemical processes occur at the end of the reaction path (question 2). Mode selective rate enhancement is not possible, contrary to the cases of symmetry-

TABLE 2: Comparison of Symmetry-Allowed Diels−Alder Reaction with the Symmetry-Forbidden FH + Ethene Cycloaddition Reaction[a]

characterization	symmetry-allowed	symmetry-forbidden
reaction type	collective reaction	domino reaction
changes in internal coordinates	many internal coordinates change collectively	single internal coordinate changes drastically and triggers a sequence of changes
curvature	no large curvature peaks close to the energy TS	high curvature peaks close to the energy TS
partitioning of the reaction path	possible using small curvature peaks	by the curvature peaks
TS region	long, not well-defined	shorter, well-defined
specific points	aromatization point spin recoupling point	bond formation point bond cleavage point
specific steps	charge-transfer step spin recoupling step bond formation step	bond formation step bond cleavage step
energy barrier	low: results from the collective changes in the structure	high: results from the chemical processes of bond cleavage/formation
change in the reaction barrier	changes in the charge-transfer step	changes in bond strength
rate enhancement	no mode selective rate enhancement possible	mode selective rate enhancement possible
hidden intermediates	not important	important
change to a nonconcerted mechanism	by asymmetric substitution; by T increase	by environmental changes

[a] Characterization of the symmetry-forbidden reaction taken from ref 7.

forbidden reactions investigated so far (question 5). The influence of the environment will be small as far as solvent effects are concerned (small dipole moment changes of the RC, see Table 1), but large in the case of a temperature raise because of the small energy difference between concerted and nonconcerted reaction (questions 6 and 9). The charge-transfer step is the key to the reaction mechanism and by this controls its stereochemistry (question 7). Any stereochemical arrangement, which suppresses a charge-transfer (asymmetric substitution by bulky groups, orbital changes due to electronegative heteroatoms) increases exchange repulsion in the region of K1 and by this also the reaction barrier. On the other hand a support of charge-transfer interactions can facilitate the reaction, which is clearly the basis of the endo rule.[1,2,14] Aromatization will be of importance in those special cases mentioned above, however, not for the prototype of the Diels−Alder reaction investigated in this work (homoaromatic stabilization by just 2.14 kcal/mol). Insofar, the aromaticity investigations of Diels−Alder TSs with the help of magnetic properties are misleading, as magnetic properties represent very sensitive antenna reflecting already small, energetically not necessarily relevant effects.

Future work has to clarify whether the mechanistic differences between a symmetry-allowed and a symmetry-forbidden reaction listed in Table 2 hold in general. However, in this work, the first step has been made to derive a general mechanistic principle, which reflects the dynamic reality of the Woodward Hoffmann rules. Particularly interesting will be symmetry-allowed reactions involving polar reaction partners. In the case of the symmetry forbidden reactions, such reactions represent mechanistically a superposition of the mechanisms of simpler reactions (e.g., a superposition of a substitution reaction and a heterolytic bond formation reaction[7]). In this connection the concept of hidden intermediates (positioned between the reaction steps) is relevant and has to be tested also for symmetry-allowed reactions. There is a large potential in these investigations and with each newly investigated reaction new insights are gained, which may give our research new turns as well as new goals.

Acknowledgment. This work was supported at Göteborg by the Swedish Natural Science Research Council (NFR). All calculations were done on the supercomputers of the Nationellt Superdatorcentrum (NSC), Linköping, Sweden. D.C. and E.K. thank the NSC for a generous allotment of computer time.

Supporting Information Available: Figures of normal-mode frequencies as a function of the reaction path length. This material is available free of charge via the Internet at http://pubs.acs.org.

References and Notes

(1) Woodward, R. B.; Hoffmann, R. *Angew. Chem., Int. Ed. Engl.* **1969**, *8*, 781.

(2) Woodward, R. B.; Hoffmann, R. *The Conservation of Orbital Symmetry*; Verlag Chemie: Weinheim, 1970.

(3) (a) Marchand, A. P.; Lehr, R. E. *Pericyclic Reactions*; Academic Press: New York, 1977. (b) Fleming, I. *Frontier Orbitals and organic Chemical Reactions*; Wiley: Chichester, 1976; p 137.

(4) Fukui, K. *Angew. Chem., Int. Ed. Engl.* **1982**, *21*, 801.

(5) Konkoli, Z.; Kraka, E.; Cremer, D. *J. Phys. Chem. A* **1997**, *112*, 1742.

(6) Kraka, E. In *Encyclopedia of Computational Chemistry*; Schleyer, PvR., Allinger, N. L., Clark, T., Gasteiger, J., Kollman, P. A., Schaefer, H. F., III, Schreiner, P. R., Eds.; Wiley: Chichester, 1998; Vol. 4, p 2437.

(7) Cremer, D.; Wu, A.; Kraka, E. *Phys. Chem. Chem. Phys.* **2001**, *3*, 674.

(8) Kraka, E.; Cremer, D. *J. Phys. Org. Chem.* **2002**, *15*, 431.

(9) Kraka, E., Wu, A., Cremer, D. Manuscript to be published.

(10) Miller, W. H.; Handy, N. C.; Adams, J. E. *J. Phys. Chem. A* **1980**, *72*, 99.

(11) (a) Fukui, K. *J. Phys. Chem.* **1970**, *74*, 4161. (b) Fukui, K. *Acc. Chem. Res.* **1981**, *14*, 363.

(12) (a) Konkoli, Z.; Cremer, D. *Int. J. Quantum Chem.* **1998**, *67*, 1. (b) Konkoli, Z.; Larsson, L. A.; Cremer, D. *Int. J. Quantum Chem.* **1998**, *67*, 11. (c) Konkoli, Z.; Larsson, L. A.; Cremer, D. *Int. J. Quantum Chem.* **1998**, *67*, 29.

(13) Cremer, D.; Larsson, L. A.; Kraka, E. In *Theoretical Organic Chemistry*; Párkányi, C., Ed.; Theoretical and Computational Chemistry, Vol. 5; Elsevier: Amsterdam, 1998; p 259.

(14) (a) Alder, K.; Stein, G. *Angew. Chem.* **1937**, *50*, 510. (b) Norton, J. A. *Chem. Rev.* **1942**, *31*, 319. (c) Woodward, R. B.; Katz, T. J. *Tetrahedron* **1959**, *5*, 70. (d) Huisgen, R.; Grashey, R.; Sauer, J. In *The Chemistry of Alkenes*; Patai, S., Ed.; Wiley, Chichester, 1964; Chapter 11, p 739. (e) Sauer, J. *Angew. Chem., Int. Ed. Engl.* **1967**, *6*, 16. (f) Sauer, J.; Sustmann, R. *Angew. Chem., Int. Ed. Engl.* **1980**, *19*, 779. (g) Fringuelli, F.; Taticchi, A. *Dienes in the Diels−Alder Reaction*; Wiley: New York, 1990. (h) March, J. *Advanced Organic Chemistry*; Wiley: New York, 1992; p 842.

(15) (a) Bernardi, F.; Bottoni, A.; Robb, M. A.; Field, M. J.; Hillier, I. H.; Guest, M. F. *J. Chem. Soc., Chem. Commun*, **1985**, 1051. (b) Houk, K. N.; Lin, Y. T.; Brown, F. K. *J. Am. Chem. Soc.* **1986**, *108*, 554. (c) Houk, K. N.; Li, Y.; Evanseck, J. D. *Angew. Chem., Int. Ed. Engl* **1992**, *31*, 682. (d) Li Y.; Houk, K. N. *J. Am. Chem. Soc.* **1993**, *115*, 7478. (e) Storer, J. W.; Raimondi, L.; Houk, K. N. *J. Am. Chem. Soc.* **1994**, *116*, 9675. (f) Houk, K. N.; Gonzales, J.; Li, Y. *Acc. Chem. Res.* **1995**, *28*, 81. (g) Jursic, B.; Zdravkovski, Z. *J. Chem. Soc. Perkin Trans. 2* **1995**, 1223. (h) Holdstein, E.; Beno, B.; Houk, K. N. *J. Am. Chem. Soc.* **1996**, *118*, 6036. (i) Karadakov, P. B.; Cooper, D. L.; Gerratt, J. *J. Am. Chem. Soc.* **1998**, *120*, 0, 3975. (j)

Sakai, S. *J. Phys. Chem. A* **2000**, *104*, 922. (k) Dinadayalane, T. C.; Vijaya, R.; Smitha, A.; Nrahari Sastry, G. *J. Phys. Chem. A* **2002**, *106*, 1627.

(16) Horn, B. A.; Herek, J. L.; Zewail, A. H. *J. Am. Chem. Soc.* **1996**, *118*, 8755.

(17) Argunents for a nonconcerted reaction were given by (a) Dewar, M. J. S.; Pierini, A. B. *J. Am. Chem. Soc.* **1984**, *106*, 203. (b) Dewar, M. J. S.; Jie, C. *Acc. Chem. Res.* **1992**, *25*, 537. (c) Firestone, R. A. *Tetrahedron* **1996**, *52*, 14459.

(18) (a) Evans, M. G.; Warhust, E. *Trans. Faraday Soc.* **1938**, *34*, 614. (b) Zimmerman, H. *Acc. Chem. Res.* **1971**, *4*, 272. (c) Dewar, M. J. S, *Angew. Chem.* **1971**, *83*, 859.

(19) Dauben, J. H.; Wilson, J. D.; Laity, J. I. I. *J. Am. Chem. Soc.* **1968**, *90*, 1390.

(20) Schleyer, P. v. R.; Maerker, C.; Dransfield, D.; Jioa, H.; van Eikema Hommes, J. R. *J. Am. Chem. Soc.* **1996**, *118*, 6317.

(21) (a) Herges, R.; Jioa, H.; Schleyer, P. v. R. *Angew. Chem., Int. Ed. Engl.* **1994**, *33*, 1376. (b) Jioa, H.; Schleyer, P. v. R. *J. Chem. Soc., Perkin Trans. 2* **1994**, 407. (c) Jioa, H.; Schleyer, P. v. R. *Angew. Chem., Int. Ed. Engl.* **1995**, *34*, 334. (d) Bernardi, F.; Celani, P.; Olivucci, M.; Robb, M. A.; Suzzi-Valli, G. *J. Am. Chem. Soc.* **1995**, *117*, 10531. (e) Jioa, H.; Schleyer, P. v. R. *J. Am. Chem. Soc.* **1995**, *117*, 11529. (f) Morao, I.; Lecea, B.; Cossio, F. P. *J. Org. Chem.* **1997**, *62*, 7033. (g) Jioa, H.; Schleyer, P. v. R. *J. Phys. Org. Chem.* **1998**, *11*, 655. (h) Morao, I.; Cossio, F. P. *J. Org. Chem.* **1999**, *64*, 1868. (i) Cossio, F. P.; Morao, I.; Jioa, H.; Schleyer, P. v. R. *J. Am. Chem. Soc.* **1999**, *121*, 6737. (j) Sawicka, D.; Wilsey, S.; Houk, K. N. *J. Am. Chem. Soc.* **1999**, *121*, 864. (k) Sawicka, D.; Li, Y.; Houk, K. N. *J. Chem. Soc., Perkin Trans. 2* **1999**, 2349.

(22) Manoharan, M.; De Proft, F.; Geerlings, P. *J. Chem. Soc., Perkin Trans.* **2000**, *2*, 1767.

(23) Bradley, A. Z.; Kociolek, M. G.; Johnson, R. P. *J. Org. Chem.* **2000**, *65*, 7134.

(24) (a) Rickborn, B. *Org. React.* **1998**, *52*, 1. (b) Rickborn, B. *Org. React.* **1998**, *53*, 223. (c) Tardy, D. C.; Ireton, R.; Gordon, A. S. *J. Am. Chem. Soc.* **1979**, *101*, 1508. (d) Kiefer, J. H.; Shah, J. N. *J. Phys, Chem.* **1987**, *91*, 3024. (e) Lewis, D. K.; Brandt, B.; Crockford, L.; Glenar, D. A.; Rauscher, G.; Rodriguez, J.; Baldwin, J. E. *J. Am. Chem. Soc.* **1993**, *115*, 11728.

(25) (a) Boger, L.; Weinberg, S. N. *Hetero Diels−Alder Methodology in Organic Synthesis*; Academic Press: New York, 1987. (b) See also, ref 14d−h. (c) Tran Huu Dau, M. E.; Flament, J.-P.; Lefour, J.-M.; Riche, C.; Gierson, D. S. *Tetrahedron Lett.* **1992**, *33*, 2343.

(26) Okamoto Y. *J. Phys. Chem. B* **2001**, *105*, 1813.

(27) Kobko, N.; Dannenberg, J. J. *J. Phys. Chem. A* **2001**, *105*, 1940.

(28) Huang, C.-H.; Tsai, L.-C.; Hu W.-P. *J. Phys. Chem. A* **2001**, *105*, 9945.

(29) For reviews, see: (a) Morokuma, K.; Kato, S. In *Potential energy characteristics for chemical reactions*; Truhlar, D. G., Ed.; Plenum: New York, 1981; p 243. (b) Miller, W. H. In *The Theory of Chemical Reaction Dynamics*; Clary, C. D., Ed.; Reidel: Dordrecht, The Netherlands, 1986; p 27. (c) Truhlar, D. G.; Garrett, B. *Annu. Rev. Phys. Chem.* **1986**, *35*, 159. (d) Truhlar, D. G.; Steckler, R.; Gordon, M. *Chem. Rev.* **1987**, *87*, 217. (e) Truhlar, D. G.; Brown, F.; Steckler, R.; Isaacson, A. D. In *The Theory of Chemical Reaction Dynamics*; Clary, C. D., Ed.; Reidel: Dordrecht, The Netherlands, 1986; p 285.

(30) Kraka, E.; Dunning, T. H., Jr. In *Advances in Molecular Electronic Structure Theory: The Calculation and Characterization of Molecular Potential Energy Surfaces*; Dunning, T. H., Jr., Ed.; JAI Press: Greenwich, CT, 1990; p 129.

(31) Page, M.; McIver, J. W. J. *J. Phys. Chem.* **1988**, *88*, 922.

(32) (a) Kato, S.; Morokuma, K. *J. Chem. Phys.* **1980**, *73*, 3900. See also: (b) Kato, S.; Morokuma, K. *J. Chem. Phys.* **1980**, *72*, 206.

(33) Konkoli, Z.; Cremer, D.; Kraka, E. *J. Comput. Chem.* **1997**, *18*, 1282.

(34) For a recent review see: Cremer, D. In *Encyclopedia of Computational Chemistry*; Schleyer, P. v. R., Allinger, N. L., Clark, T., Gasteiger, J., Kollman, P. A., Schaefer, H. F., III, Schreiner, P. R., Eds.; Wiley: Chichester, U.K., 1998; Vol. 3, p 1706.

(35) (a) Hohenberg, P.; Kohn, W. *Phys. Rev* **1994**, *136*, B864. (b) Kohn, W.; Sham, L. *J. Phys. Rev.* **1965**, *140*, A1133. See also, for example: (c) Parr, R. G.; Yang, W. *International Series of Monographs on Chemistry 16: Density-Functional Theory of Atoms and Molecules*; Oxford University Press: New York, 1989.

(36) (a) Becke, A. D. *J. Chem. Phys.* **1993**, *98*, 5648. See also: (b) Stevens, J. P.; Devlin, F. J.; Chablowski, C. F.; Frisch, M. J. *J. Phys. Chem.* **1994**, *98*, 11623.

(37) Hariharan, P. C.; Pople, J. A. *Theor. Chim. Acta* **1973**, *28*, 213.

(38) Krishnan, R.; Frisch, M.; Pople, J. A. *J. Chem. Phys.* **1980**, *72*, 4244.

(39) Raghavachari, K.; Trucks, G. W.; Pople, J. A.; Head-Gordon, M. *Chem. Phys. Lett.* **1989**, *157*, 479.

(40) Kraka, E.; Gräfenstein, J.; Gauss, J.; Filatov, M.; He, Y.; Wu, A.; Polo, V.; Reichel, F.; Olsson, L.; Konkoli, Z.; He, Z.; Cremer, D. COLOGNE 2003, Göteborg, Univeristy of Göteborg, 2003.

(41) Frisch, M. J.; Trucks, G. W.; Schlegel, H. B.; Scuseria, G. E.; Robb, M. A.; Cheeseman, J. R.; Zakrzewski, V. G.; Montgomery, J. A., Jr.; Stratmann, R. E.; Burant, J. C.; Dapprich, S.; Millam, J. M.; Daniels, A. D.; Kudin, K. N.; Strain, M. C.; Farkas, O.; Tomasi, J.; Barone, V.; Cossi M.; Cammi, R.; Mennucci, B.; Pomelli, C.; Adamo, C.; Clifford, S.; Ochterski, J.; Petersson, G. A.; Ayala, P. Y.; Cui, Q.; Morokuma, K.; Malick, D. K.; Rabuck, A. D.; Raghavachari, K.; Foresman, J. B.; Cioslowski, J.; Ortiz, J. V.; Stefanov, B. B.; Liu, G.; Liashenko, A.; Piskorz, P.; Komaromi, I.; Gomperts, R.; Martin, R. L.; Fox, D. J.; Keith, T.; Al-Laham, M. A.; Peng, C. Y.; Nanayakkara, A.; Gonzalez, C.; Challacombe, M.; Gill, P. M. W.; Johnson, B.; Chen, W.; Wong, M. W.; Andres, J. L.; Gonzalez C.; Head-Gordon, M.; Replogle, E. S.; Pople, J. A. *Gaussian98*, revision A3; Gaussian, Inc.: Pittsburgh, PA, 1998.

(42) Rowley, D.; Steiner, H. *Discuss. Faraday Soc.* **1951**, *10*, 198.

(43) Cox, J. D.; Pilcher, G. *Thermochemistry of Organic and Organometallic Compounds*; Academic Press: London, 1970.

(44) (a) Choi, C. H.; Kertesz, M.; Dobrin, S.; Michl, J. *Theor. Chem. Acc.* **1999**, *102*, 196. (b) Bock, C. W.; George, P.; Trachtman, M.; Zanger, M. *J. Chem. Soc., Perkin Trans. 2* **1979**, 26. (c) Roth, W. R.; Adamczak, O.; Breuckmann, R.; Lennartz, H.-W.; Boese, R. *Chem. Ber.* **1991**, *124*, 2499.

(45) Cremer, D.; Szabo, K. J. *Methods in Stereochemical Analysis, Conformational Behavior of Six-Membered Rings, Analysis, Dynamics, and Stereoelectronic Effects*; Juaristi, E., Ed.; VCH Publishers: New York, 1995; pp 59−134.

(46) *CRC Handbook of Chemistry and Physics on CD-ROM*, 2000 Version; Lide, D. R., Ed.; CRC Press LLC: Boca Raton, FL, 2000.

(47) Cremer, D.; Childs, R. F.; Kraka, E. In *The Chemistry of Functional Groups, The Chemistry of the Cyclopropyl Group*; Rappoport, Z., Ed.; John Wiley: New York, 1995; Vol. 2, pp 339−410.